

## MIT Open Access Articles

*Nano-kirigami with giant optical chirality*

The MIT Faculty has made this article openly available. **Please share** how this access benefits you. Your story matters.

**Citation:** Liu, Zhiguang, Huifeng Du, Jiafang Li, Ling Lu, Zhi-Yuan Li, and Nicholas X. Fang. "Nano-Kirigami with Giant Optical Chirality." *Science Advances* 4, no. 7 (July 2018): eaat4436. © 2018 The Authors

**As Published:** <http://dx.doi.org/10.1126/sciadv.aat4436>

**Publisher:** American Association for the Advancement of Science (AAAS)

**Persistent URL:** <http://hdl.handle.net/1721.1/119214>

**Version:** Final published version: final published article, as it appeared in a journal, conference proceedings, or other formally published context

**Terms of use:** Creative Commons Attribution-NonCommercial 4.0 International



## APPLIED SCIENCES AND ENGINEERING

## Nano-kirigami with giant optical chirality

Zhi-guang Liu<sup>1,4\*</sup>, Huifeng Du<sup>2\*</sup>, Jiafang Li<sup>1\*†</sup>, Ling Lu<sup>1</sup>, Zhi-Yuan Li<sup>3†</sup>, Nicholas X. Fang<sup>2†</sup>

Kirigami enables versatile shape transformation from two-dimensional (2D) precursors to 3D architectures with simplified fabrication complexity and unconventional structural geometries. We demonstrate a one-step and on-site nano-kirigami method that avoids the prescribed multistep procedures in traditional mesoscopic kirigami or origami techniques. The nano-kirigami is readily implemented by in situ cutting and buckling a suspended gold film with programmed ion beam irradiation. By using the topography-guided stress equilibrium, rich 3D shape transformation such as buckling, rotation, and twisting of nanostructures is precisely achieved, which can be predicted by our mechanical modeling. Benefiting from the nanoscale 3D twisting features, giant optical chirality is achieved in an intuitively designed 3D pinwheel-like structure, in strong contrast to the achiral 2D precursor without nano-kirigami. The demonstrated nano-kirigami, as well as the exotic 3D nanostructures, could be adopted in broad nanofabrication platforms and could open up new possibilities for the exploration of functional micro-/nanophotonic and mechanical devices.

## INTRODUCTION

Three-dimensional (3D) nanofabrication holds the key to building a large variety of micro-/nanostructures with unique and flexible functionalities, compared with their macroscopic counterparts and the 2D planar counterparts, especially in the aspects of integration and re-configuration. One promising scheme to build 3D micro-/nanostructures is the so-called kirigami or origami method (origami normally refers to the cases when a cutting process is not involved) (1, 2). This method makes use of the art and science of cutting and folding flat objects to create versatile shapes and has been of tremendous interest among both scientists and engineers because of its emerging applications in fields such as micro-/nanoelectromechanical systems (MEMSs/NEMSs) (3), energy storage systems (4), biomedical devices (5), and mechanical and photonic materials (6–9). Compared with traditional 3D micro-/nanofabrication, kirigami and origami enable the shape transformation from 2D precursors to 3D architectures without the need of precise 3D translation in direct lithography (10, 11) or accurate alignment during indirect multilayer stacking (12). Benefiting from their unique transformation characteristics such as rotation and twisting, kirigami and origami greatly enrich the 3D geometries and complexities in the frontier of both fundamental sciences (2, 13) and practical applications (3–5), compared with those from conventional techniques.

So far, the state-of-the-art kirigami- and origami-based micro-/nanofabrication methods have mainly used the differential strains between neighboring objects to achieve spontaneous curving or folding (14–17), which can be triggered by stimuli like temperature changes, volume variations, capillary forces, residual removing, etc. For example, one interesting scheme has been recently developed by using the out-of-plane compressive buckling of top precursors induced by an elastomeric support (17, 18). However, most of the schemes were involved with multiple materials or multistep processes that have to be carefully pre-designed and strictly sequenced, making it inconvenient for on-site fabrication or flexible addition. Moreover, besides the mechanical

characteristics, the unconventional 3D geometries created by kirigami at nanoscale may enable many fascinating properties such as photonic functions at optical wavelengths, which have not aroused sufficient interest. Thus, an instant, high-accuracy, and simple kirigami method, which allows one to reliably generate functional nanogeometries, is highly desirable but has yet to be explored.

Here, we introduce a one-step and on-site nano-kirigami method with nanoscale accuracy by in situ cutting and buckling a suspended gold film. By using the topography-guided stress equilibrium during global ion beam irradiation, versatile buckling, rotation, and twisting of nanostructures are simultaneously or selectively achieved. The exotic 3D structures are accurately controllable by programming ion doses, and well predictable by using an elastoplastic mechanical model. Benefiting from the nanoscale 3D twisting features, giant intrinsic optical chirality is achieved in a 3D pinwheel-like structure, in strong contrast to its 2D counterpart without nano-kirigami. The proposed concept of nano-kirigami, as well as the explored new types of 3D nanostructures, could build up novel platforms for versatile manufacturing techniques and functional structures in areas such as plasmonics, nanophotonics, optomechanics, MEMS/NEMS, etc.

## RESULTS

## Single-material kirigami

Different from mesoscopic kirigami that usually uses multiple materials, macroscopic kirigami can be simply realized by cutting flat single material and transforming it into desired shapes manually, as the paper-cut of an expandable dome illustrated in Fig. 1A. Single-material kirigami in microscopic scales, which could significantly simplify the multistep processing, is challenging because of the difficulty in finding a sophisticated enough micro-/nanomanipulator. Recent studies found that the local irradiation of thin films with focused ion beam (FIB) could introduce tensile or compressive stress for thin-film folding (19–21). However, the local irradiation-induced zero curvatures, except at the abruptly folded regions, failed in simultaneous shape transformation of multiple subunits, and were restricted by the overhead beam blocking (fig. S1), which greatly limited the flexibility in structural transformation. Moreover, from the viewpoint of topological classification, these methods belong to the elementary tree-type (open-loop) multibody system (22), in which the relative motions within each neighboring object are independent. This is relatively simple compared

Copyright © 2018  
The Authors, some  
rights reserved;  
exclusive licensee  
American Association  
for the Advancement  
of Science. No claim to  
original U.S. Government  
Works. Distributed  
under a Creative  
Commons Attribution  
NonCommercial  
License 4.0 (CC BY-NC).

<sup>1</sup>Institute of Physics, Beijing National Laboratory for Condensed Matter Physics, Chinese Academy of Sciences, Beijing 100190, China. <sup>2</sup>Department of Mechanical Engineering, Massachusetts Institute of Technology, Cambridge, MA 02139, USA. <sup>3</sup>College of Physics and Optoelectronics, South China University of Technology, Guangzhou 510640, China. <sup>4</sup>University of Chinese Academy of Sciences, Beijing 100049, China.

\*These authors contributed equally to this work.

†Corresponding author. Email: jiafangli@aphy.iphy.ac.cn (J.L.); phzyli@scut.edu.cn (Z.-Y.L.); nicfang@mit.edu (N.X.F.)

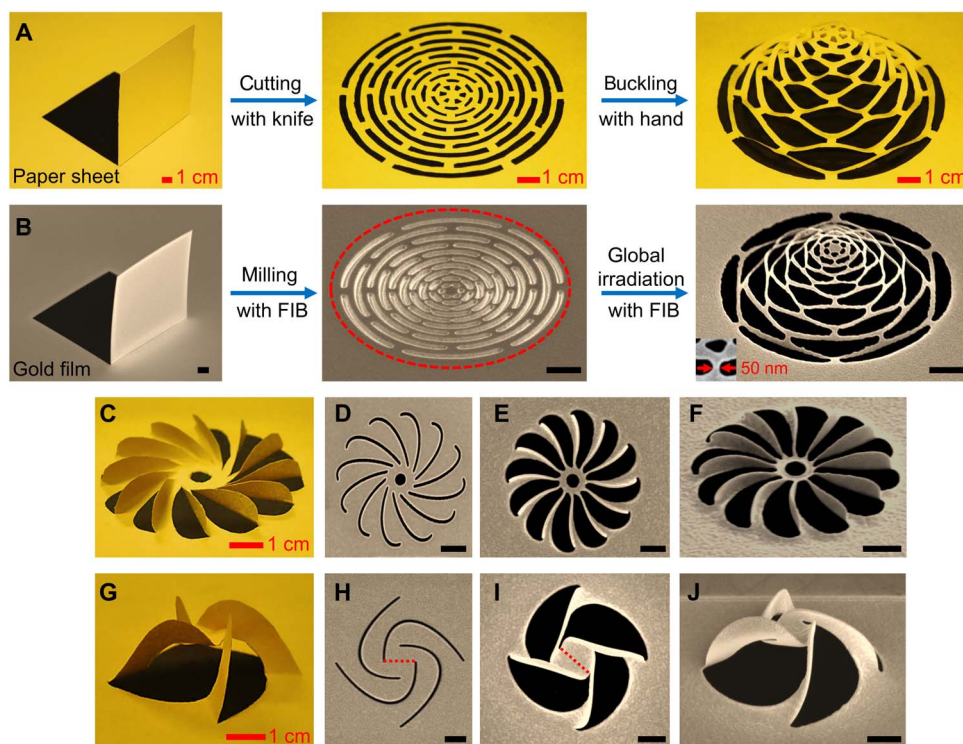


**Fig. 1. Macro-kirigami and nano-kirigami.** (A) Camera images of the paper kirigami process of an expandable dome (corresponding to a traditional Chinese kirigami named “pulling flower”). (B) SEM images of an 80-nm-thick gold film, a 2D concentric arc pattern and a 3D microdome. The high-dose FIB milling corresponds to the “cutting” process, and the global low-dose FIB irradiation of the sample area (enclosed by the dashed ellipse) corresponds to the “buckling” process in nano-kirigami. The buckling direction is downward along the FIB incident direction (fig. S1G). A 3D feature size of 50 nm is shown in the inset. (C to F) A 12-blade propeller and (G to J) a four-arm pinwheel formed in a macroscopic paper and a gold nanofilm, respectively. Top-view SEM images of the milled 2D patterns before (D and H) and after (E and I) global FIB irradiation from the top, respectively. (F and J) are the side views of (E) and (I), respectively, which are in good correspondence to the macro-kirigami in (C) and (G). The dashed lines in (H) and (I) indicate a connection between two corners of the central structure, revealing a rotation angle of  $\sim 41^\circ$  by nano-kirigami. The in situ fabrication can be programmed into one step (movie S1). Scale bars in SEM images, 1  $\mu\text{m}$ .

to the advanced kirigami in close-loop multibody systems (22), in which the relative motions within the loop become dependent; that is, a relative motion of one object affects the relative motions of the others. Actually, the interrelated shape transformation of neighboring bodies represents one of the most intrinsic natures of kirigami and provides an extra freedom toward 4D manufacturing (23), which is highly desirable but has not been implemented in nanometer accuracy with desirable functionality.

Our nano-kirigami method exhibits the features of close-loop multibody systems; that is, the final formation of the interconnected structures is determined by the overall stress equilibrium other than the isolated folding of individual components. As shown in Fig. 1B, through high-dose milling and low-dose global irradiation with gallium ion-based FIB, the paper-cut of the expandable dome is well reproduced in microscopic scale, with sub-50-nm feature size in an 80-nm-thick gold film (see Materials and Methods). This is a “buckling down” process since the rising direction of the nanostructures is along the illumination direction of the ion beam (movie S1 and fig. S1G). In more general topographic designs, 2D patterns are found to be much easier to buckle up (inverse to the ion beam illumination direction), as shown by the 12-blade propeller in Fig. 1 (C to F) and the four-arm pinwheel in Fig. 1 (G to J). It is observed that the central part of the structure can be dynamically twisted and rotated during the buckling up process, as illustrated by the rotated dashed lines in Fig. 1 (H and I), exhibiting a typical signature of the close-loop multibody systems that cannot

be achieved with tree-type fabrication methods. Moreover, all these complex structures (including other 3D structures in the following contents and in fig. S2) could be readily realized by programming the irradiation dose in one step or instantly adding in flexible orders (movie S1 and fig. S1G), which are challenging for traditional 3D fabrication methods and for the prescribed tree-type kirigami and origami methods.

### Topography-guided nano-kirigami

The main mechanism of the nano-kirigami is to use the residual stress induced by the gallium ion collisions with gold thin films (20, 21, 24), as illustrated in Fig. 2A. Specifically, when the sample area is exposed to ion irradiation, some of the gold atoms are sputtered away from the surface and the resulting vacancies cause grain coalescence (24, 25), which induces tensile stress close to the film surface. Meanwhile, some gallium ions are implanted into the film, which induces compressive stress. The two stresses occur simultaneously within  $\sim 20$  nm of the gold film (fig. S3), and the combination of them determines the overall stress within the ion beam-affected top layer, which deforms the less-affected bottom layer of gold. Our tests show that tensile stress is dominant when FIB with acceleration voltage of 30 kV is applied to a 80-nm-thick gold film (fig. S4). Therefore, the free-standing gold film in our case could be simplified into a bilayer model; that is, the top amorphous layer with tensile stress  $\sigma_t$  and the bottom layer with deformation stress  $\sigma_b$ . In such a model, when one end of the suspended structure is fixed, the top



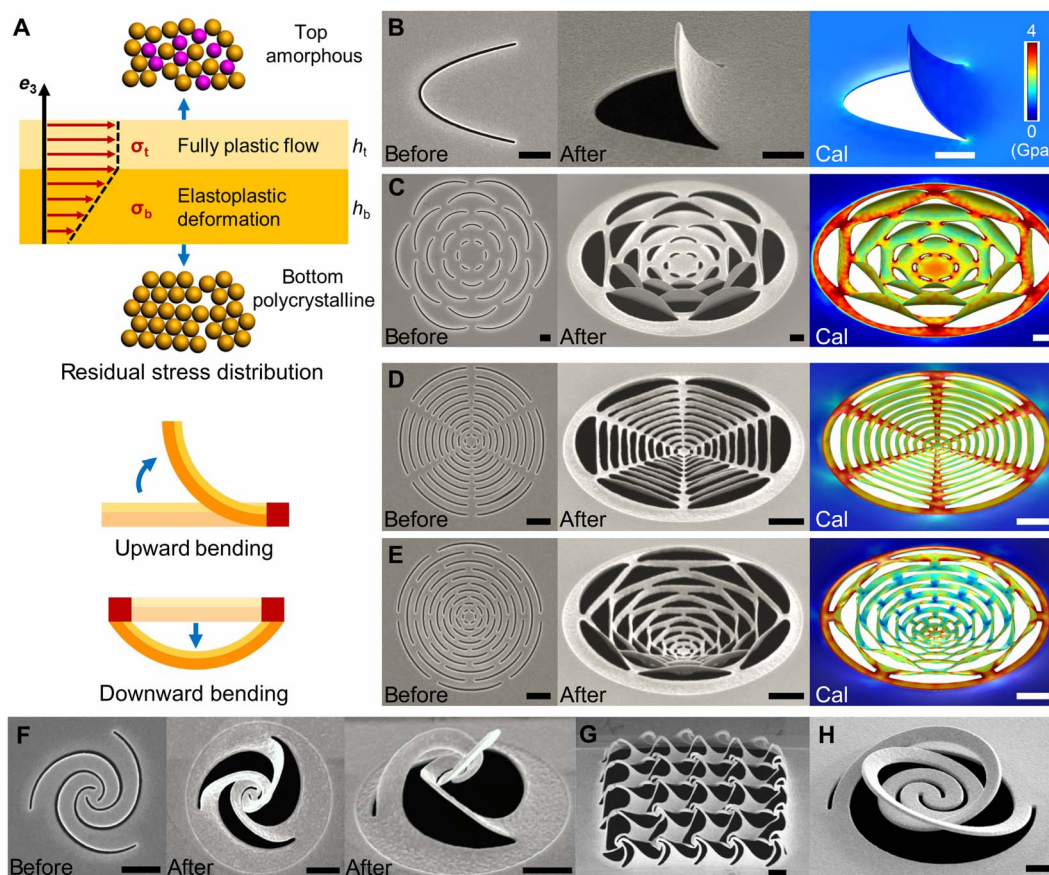


**Fig. 2. Topography-guided nano-kirigami.** (A) Schematic illustration of residual stress distribution of gold nanofilm under global ion beam irradiation. In this bilayer model (section S1), the constant tensile stress ( $\sigma_t$ ) is dominant within the top amorphous layer, and the elastic stress ( $\sigma_b$ ) is linearly distributed across the bottom polycrystalline layer. In such a case, when one edge is fixed (as noted by the red squares), the cantilever will bend upward. While both boundaries of the cantilever are fixed, the film could bend downward under the topography-guided stress equilibrium. (B and C) SEM images of (B) a tongue-like structure and (C) a flower-like structure before and after global ion beam irradiation. The calculated (Cal) structures well represent the upward bending process. (D and E) SEM images of (D) a spider web-like and (E) a concentric arc structure before and after global ion beam irradiation, showing distinctive downward buckling amplitudes under the same irradiation. (F to H) SEM images of (F) a twisted triple Fibonacci spiral, (G) window decoration-type nanobarrriers, and (H) a deformable spiral. Calculated results in (B) to (E) are displayed with the same color bar as in (B). Scale bars, 1  $\mu\text{m}$ .

tensile stress will cause the suspended structure to bend upward, like the scanning electron microscopy (SEM) images of tongue-like bending shown in Fig. 2B. This upward bending mechanism can be simultaneously applied to the multiple subunits of complex geometries, such as the upward bent “petals” of the flower-like structure in Fig. 2C (movie S2).

The precise modeling of nano-kirigami process is of critical importance since it is able to help one predict and visualize the final form of the structures. However, this is challenging in nanoscale, since the FIB-induced structural changes and material modifications are usually beyond the elastic region, and previous assumptions of purely elastic material dealing with Stoney formula are inadequate for complex structural transformation (24). We hereby develop a comprehensive mechanics model in which constant tensile stress ( $\sigma_t$ ) dominates the top amorphous layer because of the presence of plastic flow, and the bottom layer has a linear distribution of elastic stress ( $\sigma_b$ ) as a consequence of bending deformation induced by contraction of the top layer (section S1), as illustrated in Fig. 2A. In such a case, the residual stress will cause the structure to bend globally under the guidance of the initial topographies until new equilibrium morphologies are reached. Considering the

ultrasmall film thickness (50 to 80 nm), the residual stress distribution in our mechanical model could be simplified by (section S1)

$$\sigma^{\text{in-plane}}(x_3) = \begin{cases} \sigma_t = \text{const}, & h_b < x_3 \leq h_b + h_t \\ \sigma_b = \sigma_0^{\text{in-plane}} + kx_3 + o(x_3), & 0 \leq x_3 \leq h_b \end{cases} \quad (1)$$

Here,  $x_3$  is the coordinate in the thickness direction ( $e_3$ );  $h_t$  and  $h_b$  are the thicknesses of top and bottom layers, respectively;  $\sigma_t$  and  $\sigma_b$  are the residual stress in the top and bottom layers, respectively;  $\sigma_0^{\text{in-plane}}$  and  $k$  are the first- and second-order coefficient in the asymptotic expansion of stress in the bottom layer, with little  $o(x_3)$  representing the higher orders (the higher-order term is negligible considering the ultrasmall thickness of the films). With such a residual stress distribution, the fabricated structures are well reproduced by the numerical calculations, as shown in Fig. 2 (B and C), verifying the accuracy of our model.

The topography of the 2D patterns is crucial in our nano-kirigami; that is, the structural bending direction can be varied by modifying the boundaries of the 2D patterns. As illustrated in Fig. 2A, when the

boundaries of the ion beam irradiation area are changed, for example, when the multiple ends of the suspended area are fixed, the structures could possibly be buckled in a downward direction under the same residual stress. As shown in Fig. 2 (D and E), by changing the arc length and its filling ratios, the arc patterns are buckled downward after global ion beam illumination, entirely different from the upward bent petals in Fig. 2C (movie S2). Even for arc structures with the same aspect ratio and arc length, the downward buckling of the concentric arc structure in Fig. 2E is significantly larger than that of the spider web pattern in Fig. 2D (~240% larger in the calculation of fig. S6). These observations are well reproduced by the calculations in Fig. 2 (C to E) under the same stress  $\sigma_t$  and  $\sigma_b$ . The accurate modeling provides more information beyond the structural configurations, such as the final distribution of equilibrium stresses under distinctive topographies. For example, for the spider web structure in Fig. 2D, the calculated stress is mainly concentrated on the radial connection parts (26), while the concentric arc structure in Fig. 2E shows relatively uniform stress distribution. Therefore, under the same aspect ratio, the spider web structure is more fragile than the concentric arc structure when a large dose of ion beam irradiation is applied (verified in fig. S6C and movie S3). The excellent consistence between experiments and calculations proves that, in the proposed nano-kirigami, the shape transformation among neighboring parts is strongly interrelated through the stress equilibrium among multiple branches, and the resulting structures are well predictable by the mechanical model. Following this design principle, a wide range of complex 3D derivatives (fig. S2) is generated with the nano-kirigami method, such as the twisted Fibonacci spirals (Fig. 2F), the window decoration-type interconnected nanobarriers (Fig. 2G), and potentially deformable MEMS spirals (Fig. 2H) (27). These 3D exotic nanostructures have not been seen with the conventional nanofabrication techniques and may largely enrich the variety of nanophotonic devices and MEMS/NEMS in both designs and fabrications.

### Functional designs for optical chirality

While the applications of mesoscopic kirigami and origami techniques are mainly in mechanical or acoustic areas, the versatile geometries introduced by nano-kirigami open a door for nanophotonic applications. For example, from the photonic point of view, the out-of-plane twisting by nano-kirigami could help to facilitate unique electromagnetic properties such as 3D optical chirality. It is well known that intrinsic chirality, the geometric property of a structure lacking any mirror symmetry plane, exists only in 3D, and its optical response could be several orders of magnitudes higher in artificial nanostructures than that in natural chiral materials (28–31). While extrinsic optical chirality has been observed in planar 2D structures (29, 32), it typically requires strict oblique incidence, and the chiral responses are relatively weak. This is because the physical origin of the optical chirality comes from the cross-coupling between the electric and the magnetic dipoles in parallel directions (33). In the case of normal incidence, the induced magnetic dipoles in 2D structures are along the incident direction and, thus, perpendicular to the direction of electric dipoles, which makes them uncoupled and results in the lack of chirality. Therefore, 3D structures with twisting features in the propagation direction such as vertical helices (Fig. 3A) are highly desirable to realize strong optical chirality (10). However, to operate at optical or telecommunication wavelength region, the twisting elements have to be miniaturized to submicrometer scales, which is challenging because of the fabrication restrictions and, thus, limited to a few specialized techniques (34, 35). Thus, a simple 3D nanofabrication approach, with a high degree of freedom and capable of generating nanoscale twisting elements, is appealing.

Considering the exotic geometries by nano-kirigami, the design of 3D chiroptical nanostructures could be intuitively extended by rotating the vertical helices to form horizontal cross-linked helices and further evolved into a fully metallic pinwheel array, as illustrated in Fig. 3A, of which the fabrication restrictions can be readily solved by nano-kirigami (as in next paragraph). Because of the twisted loops in all directions (28), the electric field ( $E_x$ ) of the incident light could induce both electric ( $p_{x,L}$ ) and magnetic ( $m_{x,L}$ ) moments in the parallel direction (that is,  $p_{x,L}/m_{x,L}/x$ ) for the left-handed (LH) pinwheel, as illustrated in Fig. 3B. In the same manner, the electric ( $p_{y,L}$ ) and magnetic moments ( $m_{y,L}$ ) along  $y$  direction could also be induced by the magnetic field ( $H_y$ ) of the incident light (Fig. 3C). Since optical chirality is dependent on the strength of  $p\cdot m$  (36), the parallel electric and magnetic moments can interact strongly to induce pronounced optical chirality. Meanwhile, it can be seen that the direction of the induced electric and magnetic moments is highly dependent on the LH or right-handed (RH) twisting of the four arms. Specifically, in the LH pinwheel, the direction of  $p_{x,L}$  and  $p_{y,L}$  is opposite to that of  $m_{x,L}$  and  $m_{y,L}$ , respectively, which causes an LH chiroptical response (9, 28). In comparison, the direction of  $p_{x,R}$  and  $p_{y,R}$  is the same as that of  $m_{x,R}$  and  $m_{y,R}$ , respectively, revealing that the RH windmill has an RH chiral response.

To take advantage of the nano-kirigami, we intuitively designed three types of 2D spiral patterns, as shown in Fig. 3D. After applying the same residual stress with our mechanical model, 3D pinwheel structures with different height and arm width are predicted, as shown in Fig. 3D, which are geometrically equivalent to the pinwheel design in Fig. 3A. These numerical designs and results are well verified by the fabricated structures in Fig. 3E, revealing the accuracy and robustness of the proposed mechanical models. It can be seen from the SEM images that the top ends of the arms in type I pinwheel and the bottom ends of the arms in type III pinwheel are very thin. In comparison, the type II 3D pinwheel has more uniform arms, which are more stable when the structures are further scaled down (fig. S8). Therefore, to achieve desirable optical chirality with high structural stability, type II design will be used in the following studies (movie S4).

### Giant optical chirality in exotic 3D nanostructures

To realize optical chirality in telecommunication wavelengths, 2D and 3D pinwheel arrays with lattice periodicity of 1.45  $\mu\text{m}$  are successfully fabricated, as shown in Fig. 4 (A and B), where the 3D twisted arms are identified after the global ion beam illumination of the 2D patterns. It should be mentioned that, when the arm width of the pinwheel reaches around ~100 nm, the dislocation and diffusion of the gold atoms (37) under global ion irradiation start to affect the morphology of the structures. As a result, the arms of the pinwheel in Fig. 4B become relatively round compared with the twisted flat arms in Fig. 3E.

Optical chirality of these structures can be characterized by  $\chi = (n_R - n_L)/2$ , where  $n_R$  or  $n_L$  is the effective refractive index of the RH or LH circularly polarized (RCP or LCP) light. The real part of  $\chi$  causes different phase delays for RCP and LCP light and is represented by circular birefringence that results in the rotation of the linear polarization by an angle  $\theta = (n_R - n_L)\pi d/\lambda_0$ , where  $d$  is the thickness of the chiral medium, and  $\lambda_0$  is the light wavelength in vacuum (29). The imaginary part of  $\chi$  corresponds to circular dichroism (CD), which causes different absorption losses for RCP and LCP waves.

Optical measurements show that the 2D structure in Fig. 4A does not have any CD and circular birefringence effect under normal incidence (Fig. 4, D and E), as expected because of its 2D nature. In comparison, the experimental 3D pinwheel structure in Fig. 4 (B and C)

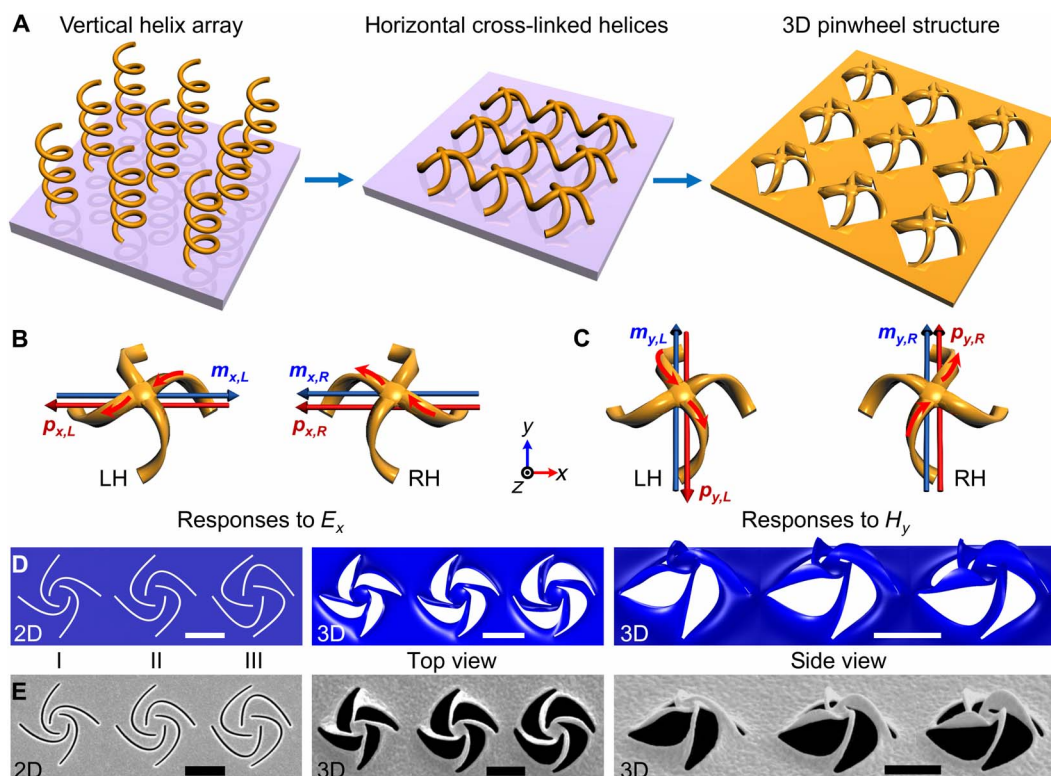


**Fig. 3. Functional designs for optical chirality.** (A) Schematic of vertical helix array, horizontal cross-linked helices, and a 3D pinwheel array [the 3D pinwheel can also be treated as two cross-linked and twisted ohm-shaped circuits (28) standing onto a metallic hole array]. (B and C) Illustration of the responses to the (B) electric field ( $E_x$ ) and (C) magnetic field ( $H_y$ ) of incident light for the LH and RH twisted pinwheels, respectively. The direction of induced electric moments  $p_{ij}$  ( $i = x$  or  $y$ ,  $j = L$  or  $R$ ) and magnetic moments  $m_{ij}$  at the center parts is noted by the arrows for LH ( $j = L$ ) and RH ( $j = R$ ) pinwheels, respectively (generalized from the simulated results in fig. S7). (D) Numerical designs of three 2D spiral patterns (types I, II, and III), the top view, and side view of the numerically predicted 3D structures, respectively, under the same residual stress distribution. (E) SEM images of the fabricated 2D patterns and corresponding 3D pinwheels after global ion irradiation with the same doses, agreeing excellently with the numerical predictions. Scale bars, 1  $\mu\text{m}$ .

exhibits clear CD effects, in which the CD spectra of LH and RH 3D structures show nearly opposite signs with similar amplitudes, as the curves plotted in Fig. 4D. This is in good agreement with the analysis in Fig. 3 (B and C). Meanwhile, pronounced circular birefringence versus wavelength is observed, as plotted in Fig. 4 (E and F), in which the rotation angle ( $\theta$ ) of the linear polarization increases markedly in the long wavelength region. The polarization rotation angles reach  $\sim 90^\circ$  and  $\sim 135^\circ$  at 1.70 and 1.95  $\mu\text{m}$ , respectively, without making the polarization state elliptical (Fig. 4F). Considering the overall structural thickness of  $\sim 430$  nm (including the bottom layer), such circular birefringence is giant compared to the statistics of chiral metamaterials and planar structures in the literature (36). The experimental results agree well with the calculations and unambiguously show that, by simply introducing 3D twisting structures through nano-kirigami, the optical chirality can be significantly enhanced compared with that of the 2D counterpart. Meanwhile, it shows that compared to other chiral structures with multilayer or twisting designs in terahertz, gigahertz, or mid-infrared wavelengths, the nano-kirigami has nanoscale accuracy while markedly simplifying the fabrication difficulty without reducing the structural complexity (33).

## DISCUSSION

We have demonstrated a novel 3D nanofabrication technology based on an on-site nano-kirigami method that is applicable by programming the dosages of the ion beam irradiation in one step. On the basis of

the deliberate engineering of the topography-guided stress equilibrium of gold nanostructures during ion beam irradiation, versatile 3D shape transformations of nanoscale structures were simultaneously and selectively achieved. Compared with traditional 3D nanofabrication techniques such as direct writing (10) and multilayer stacking (12), the nano-kirigami method significantly simplifies the fabrication complexity while retaining the diversity and functionality of 3D nanostructures. Meanwhile, it overcomes the prescribed and multistep procedures in traditional mesoscopic kirigami and origami methods by instantly cutting and buckling nanofilms with the same ion beams, which makes it convenient to perform nanometer-accurate kirigami in one step. The exotic 3D structures have been well predicted by using an elastoplastic mechanical model, which not only provides a reliable tool for feasibility tests and internal stress analysis but also opens a window for inverse designs of desirable functionalities. Finally, as a functionalization of the nanoscale 3D twisting features, an exotic gold pinwheel with giant optical chirality has been realized in telecommunication wavelengths. Since the 3D pinwheels have fourfold ( $C_4$ ) rotational symmetry on the  $z$  axis, the chirality is expected as uniaxial for normal incident light (28). The strong chiroptical responses were not observed in the corresponding 2D counterpart, unambiguously revealing the significance brought by the nano-kirigami. It should be noted that if the  $C_4$  pinwheels are arranged in triangular lattices with sixfold rotational ( $C_6$ ) lattice symmetry, then the resulting 3D structures will have twofold rotational ( $C_2$ ) symmetry. In such a case, circular polarization conversion can be observed



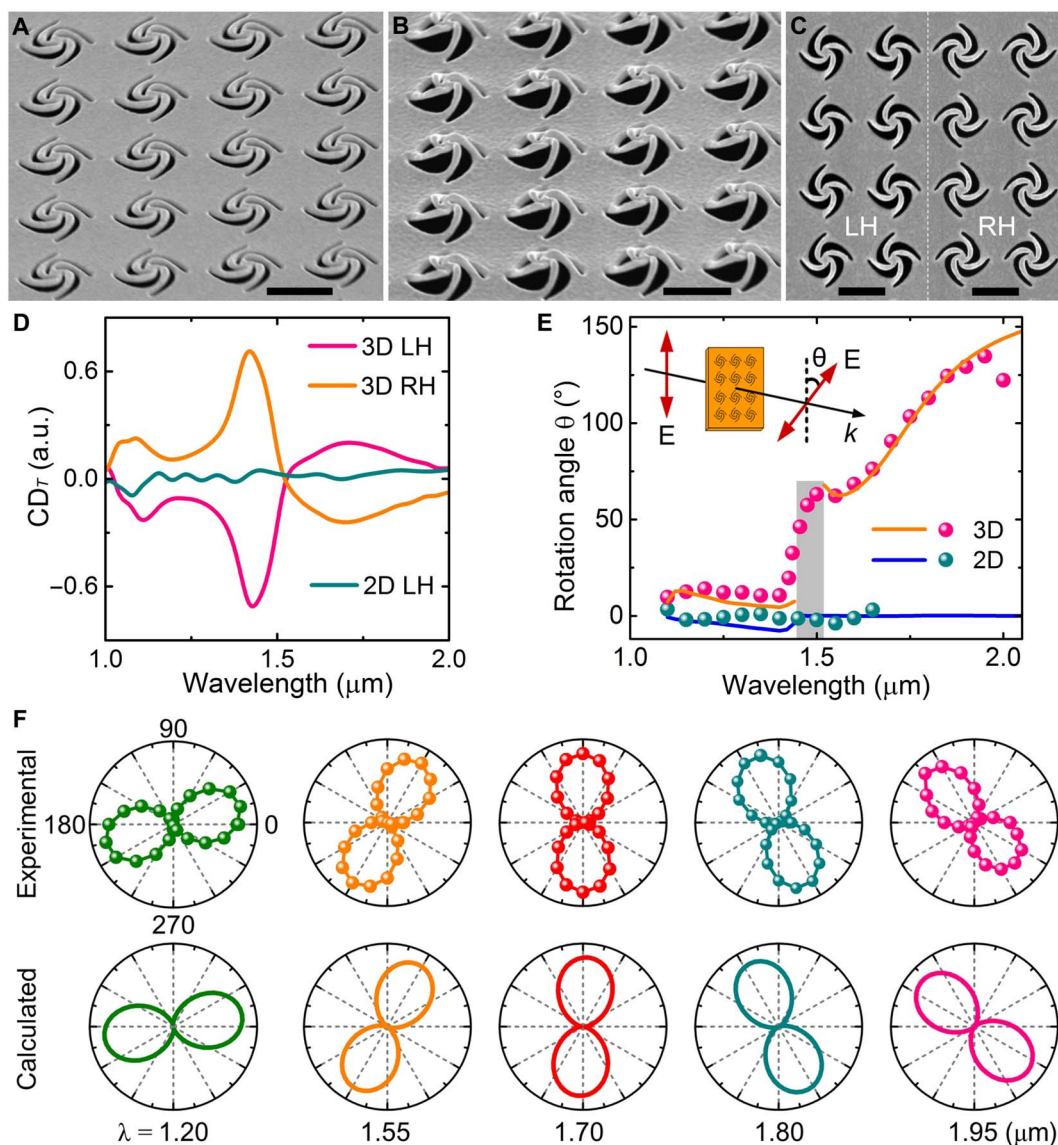


**Fig. 4. Giant optical chirality.** (A and B) SEM images of (A) 2D and (B) 3D pinwheel array with periodicity of 1.45  $\mu\text{m}$ . The height of the 3D pinwheels is about 380 nm. (C) Top-view SEM images of LH and RH 3D pinwheel arrays. Scale bars, 1  $\mu\text{m}$ . (D) Measured CD in transmission [defined as  $CD_T = (T_L - T_R)/(T_L + T_R)$ ] versus wavelength for 2D LH, 3D LH, and 3D RH pinwheels, respectively. a.u., arbitrary units. (E) Measured (circular points) and calculated (solid lines) linear polarization rotation angle ( $\theta$ ) versus wavelength for 3D and 2D LH pinwheels, respectively. The unrealistic abrupt peaks around 1.45  $\mu\text{m}$  in calculation are not shown for clearance because of the inaccurate retrieval of polarization states at nearly zero transmission at Wood's anomaly (see full calculated data in fig. S9). Inset: Schematic of the linear polarization rotation. (F) Polar plot of (top) experimental and (bottom) calculated transmission versus detection polarization angle at specific wavelengths under x-polarized incidence for the 3D LH pinwheels. Nearly linearly polarized states are observed. In comparison, for wavelengths in the strong CD region (around 1.45  $\mu\text{m}$ ), the measured transmission of light exhibits elliptical polarization states (fig. S9H). Spectra are measured from 1.1 to 2  $\mu\text{m}$  because of the restriction of the quarter-wave plate (see Materials and Methods).

at a certain wavelength region. The studies in this aspect are interesting and deserve profound investigation.

One distinctive feature of our nano-kirigami method is that, during the global ion beam irradiation, the thinning and transformation of nanofilm, accompanied by the atom dislocations and diffusions, occur simultaneously across the whole sample region other than localized at the sequential folding areas. Therefore, the topography-guided stress equilibrium among subunits, instead of individual folding, determines the final structural configuration. Compared to the FIB-induced deposition method (38, 39), this proof-of-concept nanofabrication could

be applied to a wide variety of suspended thin-film materials [such as aluminum and commercial silicon nitride thin films in fig. S10 (A and B)] and to other ion-based etching or implant systems to achieve large-scale fabrications, although the specific stress responses may be different from those of gold (section S3). The geometries of the enabled 3D structures could also be extended to other types, such as three-arm 3D pinwheels that break the center-inversion symmetry (fig. S10, C and D). Moreover, the suspending features endow the 3D nanostructures with potential applications on reconfigurable nanophotonic and optomechanical devices by engineering the suspended subunits, such as

the scheme used by commercial digital micromirror devices in digital light processing projection and related 3D printing industry. Therefore, our work here not only builds up a new nanofabrication concept and platform for diverse structural geometries and functionalities but also opens up new possibilities for the active configuration of versatile micro-/nanophotonic and electronic devices.

## MATERIALS AND METHODS

### Numerical simulations

The transmission spectra and electromagnetic field distributions of the 2D and 3D gold structures were simulated by using the finite element method. The current distributions were obtained by using a current density monitor in commercial software package CST Microwave Studio based on the finite integration method. Periodic boundary conditions along the  $x$ - and  $y$ -axis direction were applied to the unit cell of the simulated structures. Incident plane wave was incident along the  $z$ -axis direction, which was identical to the conditions in experiments. The refractive index and extinction coefficient of gold were described by the Lorentz-Drude model. The thickness of the target nanostructures after nano-kirigami transformation was set to 50 nm in simulations unless otherwise specified, which was under the consideration of the sputtering effect during the global ion beam irradiation and confirmed in SEM characterizations. The deformed configurations of 3D nano-kirigami architectures were calculated with finite element software SIMULIA Abaqus FEA and COMSOL Multiphysics. User-defined subroutines were implemented for applying the nonuniform residual stress field to trigger global buckling of nanofilms. More details related to modeling can be found in sections S1 and S2.

### Sample fabrications

All the 3D structures were fabricated with a dual-beam FIB/SEM system (FEI Helios 600i) on self-supporting gold nanofilms. The 80-nm-thick gold film suspended on copper grid was prepared by lift-off process in previous studies and directly used here (40). To avoid unwanted film fluctuations, multiple flat and clean sample areas satisfying the fabrication requirements were carefully selected from more than 100 meshes on the copper grid. The maximum size of each sample area is  $\sim 100 \mu\text{m} \times 100 \mu\text{m}$ , which is limited by the mesh size. For large-scale fabrication, suspended nanofilms with desirable flatness are commercially available, such as the silicon nitride film window ( $500 \mu\text{m} \times 500 \mu\text{m} \times 50 \text{nm}$  in size; Norcada) used in fig. S10B. The nano-kirigami method includes a two-dosage ion beam irradiation. First, the 2D patterns were directly cut by the FIB under high doses of  $1.9 \times 10^8$  ions/ $\mu\text{m}^2$  ( $>600 \text{pC}/\mu\text{m}^2$ ). Subsequently, global ion beam irradiation was conducted by frame-scanning the effective sample area with relative low doses of 10 to  $40 \text{pC}/\mu\text{m}^2$  without particular alignment. The whole process could be programmed into one step and in situ monitored by the SEM (see movie S1). The acceleration voltage and current beam of  $\text{Ga}^+$  were set at 30 kV and 24 pA, respectively, if not mentioned. In such a case, the nano-kirigami took a few minutes for most of the single structures. For an array of 3D pinwheels with lattice period of  $1.45 \mu\text{m}$  and sample area of  $30 \mu\text{m} \times 30 \mu\text{m}$ , the fabrication time was less than 30 min. Because of the large scales of the structure, the overall fabrication resolution was about 20 nm.

### Optical characterizations

The optical measurements were performed using a homemade spectroscopy system designed to characterize samples with small sizes. For transmission spectral measurement, white light from tungsten

halogen source (HL-2000, Ocean Optics) or supercontinuum light sources (SC400-4, Fianium) was collimated and confined to proper beam size, which was then weakly focused onto the sample by a near-infrared (NIR) objective lens [ $\times 10$ , 0.25 numerical aperture (NA); Olympus]. The transmitted signals were collected using another NIR objective lens ( $\times 100$ , NA 0.9; Olympus) and delivered to a spectrometer (SP-2300, Princeton Instruments) equipped with a liquid nitrogen-cooled charge-coupled device (CCD) detector (PyLoN-IR). An NIR CCD camera (XS-4406, Xenics) was set within the switching optical path for imaging. For measurement of CD, a linear polarizer (650 to 2000 nm; Thorlabs) and a quarter-wave plate (1100 to 2000 nm; Thorlabs) were inserted into the input optical path at specific orientations. Therefore, the spectra in this work were mainly focused on wavelength range from 1100 to 2000 nm. Linear polarization rotation experiments were conducted by varying the detection polarization (linear polarizer, 650 to 2000 nm; Thorlabs) at every  $15^\circ$  under linearly polarized incidence.

## SUPPLEMENTARY MATERIALS

Supplementary material for this article is available at <http://advances.sciencemag.org/cgi/content/full/4/7/eaat4436/DC1>

Section S1. Mechanical modeling

Section S2. Optical modeling

Section S3. Extension of nano-kirigami to other materials and geometries

Fig. S1. Illustration of the overhead ion beam blocking and comparison between local and global ion beam irradiation.

Fig. S2. Exotic 3D structures fabricated by nano-kirigami.

Fig. S3. SRIM software simulation results.

Fig. S4. Ion beam dosage test.

Fig. S5. Schematic of the bottom layer under elastoplastic deformation.

Fig. S6. Comparison between web-like structures of different topographies after nano-kirigami.

Fig. S7. Origin of the chirality in 3D pinwheel structures.

Fig. S8. Structural designs for optical chirality.

Fig. S9. Numerical calculations and comparison with experiments.

Fig. S10. Extension of nano-kirigami to other platforms.

Movie S1. Nano-kirigami of different structures by programming ion beam irradiation in one step.

Movie S2. Upward and downward buckling with nano-kirigami.

Movie S3. Structural evolution of different web-like structures under nano-kirigami.

Movie S4. Simultaneous upward buckling of an array of pinwheel structures.

## REFERENCES AND NOTES

- G. P. Collins, Science and culture: Kirigami and technology cut a fine figure, together. *Proc. Natl. Acad. Sci. U.S.A.* **113**, 240–241 (2016).
- S. Perks, Flat-pack physics. *Phys. World* **28**, 21 (2015).
- J. Rogers, Y. G. Huang, O. G. Schmidt, D. H. Gracias, Origami MEMS and NEMS. *MRS Bull.* **41**, 123–129 (2016).
- J. Deng, H. Ji, C. Yan, J. Zhang, W. Si, S. Baunack, S. Oswald, Y. Mei, O. G. Schmidt, Naturally rolled-up C/Si/C trilayer nanomembranes as stable anodes for lithium-ion batteries with remarkable cycling performance. *Angew. Chem. Int. Ed.* **52**, 2326–2330 (2013).
- K. Kuribayashi, K. Tsuchiya, Z. You, D. Tomus, M. Umamoto, T. Ito, M. Sasaki, Self-deployable origami stent grafts as a biomedical application of Ni-rich TiNi shape memory alloy foil. *Mater. Sci. Eng. A* **419**, 131–137 (2006).
- J. L. Silverberg, A. A. Evans, L. McLeod, R. C. Hayward, T. Hull, C. D. Santangelo, I. Cohen, Using origami design principles to fold reprogrammable mechanical metamaterials. *Science* **345**, 647–650 (2014).
- M. K. Blees, A. W. Barnard, P. A. Rose, S. P. Roberts, K. L. McGill, P. Y. Huang, A. R. Ruyack, J. W. Kevek, B. Kobrin, D. A. Muller, P. L. McEuen, Graphene kirigami. *Nature* **524**, 204–207 (2015).
- A. Lamoureux, K. Lee, M. Shlian, S. R. Forrest, M. Shtein, Dynamic kirigami structures for integrated solar tracking. *Nat. Commun.* **6**, 8092 (2015).
- Z. Wang, L. Jing, K. Yao, Y. Yang, B. Zheng, C. M. Soukoulis, H. Chen, Y. Liu, Origami-based reconfigurable metamaterials for tunable chirality. *Adv. Mater.* **29**, 1700412 (2017).



10. J. K. Gansel, M. Thiel, M. S. Rill, M. Decker, K. Bade, V. Saile, G. von Freymann, S. Linden, M. Wegener, Gold helix photonic metamaterial as broadband circular polarizer. *Science* **325**, 1513–1515 (2009).
  11. M. D. Turner, M. Saba, Q. Zhang, B. P. Cumming, G. E. Schröder-Turk, M. Gu, Miniature chiral beamsplitter based on gyroid photonic crystals. *Nat. Photonics* **7**, 801–805 (2013).
  12. N. Liu, H. Guo, L. Fu, S. Kaiser, H. Schweizer, H. Giessen, Three-dimensional photonic metamaterials at optical frequencies. *Nat. Mater.* **7**, 31–37 (2008).
  13. A. Rafsanjani, K. Bertoldi, Buckling-induced kirigami. *Phys. Rev. Lett.* **118**, 084301 (2017).
  14. Z. Chen, G. Huang, I. Trase, X. Han, Y. Mei, Mechanical self-assembly of a strain-engineered flexible layer: Wrinkling, rolling, and twisting. *Phys. Rev. Appl.* **5**, 017001 (2016).
  15. E. A. Peraza-Hernandez, D. J. Hartl, R. J. Malak Jr., D. C. Lagoudas, Origami-inspired active structures: A synthesis and review. *Smart Mater. Struct.* **23**, 094001 (2014).
  16. L. Xu, T. C. Shyu, N. A. Kotov, Origami and kirigami nanocomposites. *ACS Nano* **11**, 7587–7599 (2017).
  17. Y. Zhang, F. Zhang, Z. Yan, Q. Ma, X. Li, Y. Huang, J. A. Rogers, Printing, folding and assembly methods for forming 3D mesostructures in advanced materials. *Nat. Rev. Mater.* **2**, 17019 (2017).
  18. S. Xu, Z. Yan, K.-I. Jang, W. Huang, H. Fu, J. Kim, Z. Wei, M. Flavin, J. McCracken, R. Wang, A. Badea, Y. Liu, D. Xiao, G. Zhou, J. Lee, H. U. Chung, H. Cheng, W. Ren, A. Banks, X. Li, U. Paik, R. G. Nuzzo, Y. Huang, Y. Zhang, J. A. Rogers, Assembly of micro/nanomaterials into complex, three-dimensional architectures by compressive buckling. *Science* **347**, 154–159 (2015).
  19. W. J. Arora, S. Sijbrandij, L. Stern, J. Notte, H. I. Smith, G. Barbastathis, Membrane folding by helium ion implantation for three-dimensional device fabrication. *J. Vac. Sci. Technol. B* **25**, 2184 (2007).
  20. W. J. Arora, H. I. Smith, G. Barbastathis, Membrane folding by ion implantation induced stress to fabricate three-dimensional nanostructures. *Microelectron. Eng.* **84**, 1454–1458 (2007).
  21. A. J. Cui, Z. Liu, J. Li, T. H. Shen, X. Xia, Z. Li, Z. Gong, H. Li, B. Wang, J. Li, H. Yang, W. Li, C. Gu, Directly patterned substrate-free plasmonic “nanograting” structures with unusual Fano resonances. *Light Sci. Appl.* **4**, e308 (2015).
  22. T. Buchner, “Kinematics of 3D Folding Structures for Nanostructured Origami<sup>TM</sup>,” thesis, Massachusetts Institute of Technology (2003).
  23. F. Momeni, N. S. M. M. Hassani, X. Liu, J. Ni, A review of 4D printing. *Mater. Des.* **122**, 42–79 (2017).
  24. M. J. Samayoa, M. A. Haque, P. H. Cohen, Focused ion beam irradiation effects on nanoscale freestanding thin films. *J. Micromech. Microeng.* **18**, 095005 (2008).
  25. W. D. Nix, B. M. Clemens, Crystallite coalescence: A mechanism for intrinsic tensile stresses in thin films. *J. Mater. Res.* **14**, 3467–3473 (1999).
  26. Z. Qin, B. G. Compton, J. A. Lewis, M. J. Buehler, Structural optimization of 3D-printed synthetic spider webs for high strength. *Nat. Commun.* **6**, 7038 (2015).
  27. T. Kan, A. Isozaki, N. Kanda, N. Nemoto, K. Konishi, H. Takahashi, M. Kuwata-Gonokami, K. Matsumoto, I. Shimoyama, Enantiomeric switching of chiral metamaterial for terahertz polarization modulation employing vertically deformable MEMS spirals. *Nat. Commun.* **6**, 8422 (2015).
  28. R. Zhao, L. Zhang, J. Zhou, T. Koschny, C. M. Soukoulis, Conjugated gammadion chiral metamaterial with uniaxial optical activity and negative refractive index. *Phys. Rev. B* **83**, 035105 (2011).
  29. Z. Wang, F. Cheng, T. Winsor, Y. Liu, Optical chiral metamaterials: A review of the fundamentals, fabrication methods and applications. *Nanotechnology* **27**, 412001 (2016).
  30. S. P. Rodrigues, S. Lan, L. Kang, Y. Cui, P. W. Panuski, S. Wang, A. M. Urbas, W. Cai, Intensity-dependent modulation of optically active signals in a chiral metamaterial. *Nat. Commun.* **8**, 14602 (2017).
  31. M. Hentschel, M. Schäferling, X. Duan, H. Giessen, N. Liu, Chiral plasmonics. *Sci. Adv.* **3**, e1602735 (2017).
  32. E. Plum, X.-X. Liu, V. A. Fedotov, Y. Chen, D. P. Tsai, N. I. Zheludev, Metamaterials: Optical activity without chirality. *Phys. Rev. Lett.* **102**, 113902 (2009).
  33. S. Zhang, Y.-S. Park, J. Li, X. Lu, W. Zhang, X. Zhang, Negative refractive index in chiral metamaterials. *Phys. Rev. Lett.* **102**, 023901 (2009).
  34. J. Kaschke, M. Wegener, Optical and infrared helical metamaterials. *Nanophotonics* **5**, 510–523 (2016).
  35. M. Esposito, V. Tasco, M. Cuscutà, F. Todisco, A. Benedetti, I. Tarantini, M. De Giorgi, D. Sanvitto, A. Passaseo, Nanoscale 3D chiral plasmonic helices with circular dichroism at visible frequencies. *ACS Photonics* **2**, 105–114 (2015).
  36. A. Y. Zhu, W. T. Chen, A. Zaidi, Y.-W. Huang, M. Khorasaninejad, V. Sanjeev, C.-W. Qiu, F. Capasso, Giant intrinsic chiro-optical activity in planar dielectric nanostructures. *Light Sci. Appl.* **7**, 17158 (2018).
  37. C. Li, L. Zhao, Y. Mao, W. Wu, J. Xu, Focused-ion-beam induced Rayleigh-Plateau instability for diversiform suspended nanostructure fabrication. *Sci. Rep.* **5**, 8236 (2015).
  38. S. Matsui, T. Kaito, J.-I. Fujita, M. Komuro, K. Kanda, Y. Haruyama, Three-dimensional nanostructure fabrication by focused-ion-beam chemical vapor deposition. *J. Vac. Sci. Technol. B* **18**, 3181–3184 (2000).
  39. I. Utke, P. Hoffmann, J. Melngailis, Gas-assisted focused electron beam and ion beam processing and fabrication. *J. Vac. Sci. Technol. B* **26**, 1197–1276 (2008).
  40. Z. G. Liu, Z. Liu, J. Li, W. Li, J. Li, C. Gu, Z.-Y. Li, 3D conductive coupling for efficient generation of prominent Fano resonances in metamaterials. *Sci. Rep.* **6**, 27817 (2016).
- Acknowledgments:** We thank Z. Liu, W. Li, A. Jin, C. Tang, J. Li, and C. Gu from the Laboratory of Microfabrication, Institute of Physics, Chinese Academy of Sciences for assistance in FIB facilities and G. X. Li from Southern University of Science and Technology for useful discussions. **Funding:** This work was supported by the National Key R&D Program of China under grant no. 2017YFA0303800; the National Natural Science Foundation of China under grant nos. 61475186, 61675227, and 11434017; and the visiting program of Chinese Scholarship Council under grant no. 201704910310. N.X.F. and H.D. acknowledge the financial support from Air Force Office of Scientific Research Multidisciplinary Research Program of the University Research Initiative (award FA9550-12-1-0488, “Quantum Metaphotonics and Quantum Metamaterials”) and from KAUST-MIT agreement no. 2950 (“Metamaterials by deep subwavelength non-Hermitian engineering”). **Author contributions:** Z.L. and J.L. developed the nano-kirigami methods, fabricated the sample, conducted the optical measurements, and analyzed the data; H.D. and N.X.F. performed the mechanical modeling and contributed to the studies on fabrication mechanism, optical chirality, and potential inverse designs; Z.L. performed the numerical simulations on optical chirality; J.L. and Z.-Y.L. conceived the concept of one-step nanofabrication; J.L. and L.L. conceived the concept of nano-kirigami and contributed to the structural designs; and J.L. supervised the whole project. All authors participated in the project discussion and manuscript preparation. **Competing interests:** The authors declare that they have no competing interests. **Data and materials availability:** All data needed to evaluate the conclusions in the paper are present in the paper and/or the Supplementary Materials. Additional data related to this paper may be requested from the authors.
- Submitted 27 February 2018  
Accepted 29 May 2018  
Published 6 July 2018  
10.1126/sciadv.aat4436
- Citation:** Z. Liu, H. Du, J. Li, L. Lu, Z.-Y. Li, N. X. Fang, Nano-kirigami with giant optical chirality. *Sci. Adv.* **4**, eaat4436 (2018).

## Nano-kirigami with giant optical chirality

Zhiguang Liu, Huifeng Du, Jiafang Li, Ling Lu, Zhi-Yuan Li and Nicholas X. Fang

*Sci Adv* 4 (7), eaat4436.  
DOI: 10.1126/sciadv.aat4436

### ARTICLE TOOLS

<http://advances.sciencemag.org/content/4/7/eaat4436>

### SUPPLEMENTARY MATERIALS

<http://advances.sciencemag.org/content/suppl/2018/07/02/4.7.eaat4436.DC1>

### REFERENCES

This article cites 39 articles, 5 of which you can access for free  
<http://advances.sciencemag.org/content/4/7/eaat4436#BIBL>

### PERMISSIONS

<http://www.sciencemag.org/help/reprints-and-permissions>

Use of this article is subject to the [Terms of Service](#)

---

*Science Advances* (ISSN 2375-2548) is published by the American Association for the Advancement of Science, 1200 New York Avenue NW, Washington, DC 20005. 2017 © The Authors, some rights reserved; exclusive licensee American Association for the Advancement of Science. No claim to original U.S. Government Works. The title *Science Advances* is a registered trademark of AAAS.